ADVANCED MATERIALS
www.advmat.de

Record Efficiency of β-Phase PVDF-MXene Composites in Thin-Film Dielectric Capacitors

James FitzPatrick, Sumit Bera, Alex Inman, Alessandra Cabrera, Teng Zhang, Tetiana Parker, Bita Soltan Mohammadlou, Iryna Roslyk, Stefano Ippolito, Kateryna Shevchuk, Sujit A. Kadam, Nihar R. Pradhan, and Yury Gogotsi**

Polyvinylidene fluoride (PVDF) is a semicrystalline polymer used in thin-film dielectric capacitors because of its inherently high dielectric constant and low loss tangent. Its dielectric constant can be increased by the formation and alignment of its β-phase crystalline structure, which can be facilitated by 2D nanofillers. 2D carbides and nitrides, MXenes, are promising candidates due to their notable dielectric permittivity and ability to increase interfacial polarization. Still, their mixing is challenging due to weak interfacial interactions and poor dispersibility of MXenes in PVDF. This work explores a novel method for delaminating $Ti_3C_2T_x$ MXene directly into organic solvents while maintaining flake size and quality, as well as the use of a non-solvent-induced phase separation method for producing both dense and porous PVDF-MXene composite films. A deeper understanding of dielectric behavior in these composites is reached by examining MXenes with both mixed and pure chlorine terminations in PVDF matrices. Thin-film capacitors fabricated from these composites display ultrahigh discharge energy density, exceeding 45 J cm^{-3} with 95% efficiency. The PVDF-MXene composites are also processed using a green and sustainable solvent, propylene carbonate.

1. Introduction

Thin-film capacitors offer a promising energy storage solution due to their rapid charge/discharge rates, cycling stability, and power density.[1,2] Dielectric polymer films are very attractive for this application due to their high breakdown voltage and dielectric permittivity, two factors crucial to determining the maximum energy density of a dielectric.[3] However, many polymer systems still fall short in terms of discharge energy density and efficiency compared to alternative energy storage methods. Polyvinylidene fluoride (PVDF) is a semicrystalline fluoropolymer that has been widely researched for this application due to its inherently high dielectric constant, up to 10 as compared to 2–4 in other polymers, as well as ease of processing and chemical resistance.[4,5] Even though pristine PVDF films typically reach a discharge density of 5–10 J cm^{-3}, which is much higher than commercially available biaxially oriented polypropylene films at 1–3 J cm^{-3},[5] these values are still low compared to electrochemical capacitors. Several methods can be employed to increase the dielectric permittivity and energy density of PVDF films.

PVDF forms five distinct crystal polymorphs: α, β, γ, δ, and ϵ, with the β-phase being of particular interest due to its highly polar structure and improved permittivity.[6] While not as energetically favorable to form as the nonpolar α-phase, there has been much research demonstrating the role that processing methods, solvent selection, and nanofiller inclusion can play in increasing the content and orientation of the β-phase.[7–9] In particular, PVDF dissolved in a highly polar solvent such as propylene carbonate (PC) has been shown to form almost entirely β-phase in its crystalline portion when cast using a non-solvent induced phase separation (NIPS) method.[7] The inclusion of low-dimensional nanofillers can not only improve dielectric permittivity within PVDF and provide interfacial polarization but also align the polymer's β-phase chains to enhance overall permittivity.[10,11] Many attempts have been made to utilize nanomaterials to enhance the dielectric permittivity of PVDF. Jiang et al.[12] increased the energy density of PVDF films by integrating boron nitride nanosheets and barium zirconate titanate nanofibers in a gradient structure, achieving over double the discharge energy density of pristine PVDF at 23.4 J cm^{-3} and a staggering discharge efficiency of 83%. Bao et al.[13] utilized negatively charged nanosheets of $Ca_2Nb_3O_{10}$ to slow down electron transport in the polymer matrix and maintain a high breakdown voltage, effectively reaching an energy density of 36.2 J cm^{-3} with an efficiency of 61.2%. Accordingly, 2D nanosheets

J. FitzPatrick, A. Inman, A. Cabrera, T. Zhang, T. Parker, B. S. Mohammadlou, I. Roslyk, S. Ippolito, K. Shevchuk, Y. Gogotsi
A.J. Drexel Nanomaterials Institute and Department of Material Science and Engineering
Drexel University
3141 Chestnut St., Philadelphia, PA 19104, USA
E-mail: gogotsi@drexel.edu

S. Bera, S. A. Kadam, N. R. Pradhan
Layered Materials and Device Physics Lab
Department of Chemistry, Physics and Atmospheric Science
Jackson State University
1400 John R. Lynch Street, Jackson, MS 39217, USA
E-mail: nihar.r.pradan@jsums.edu

The ORCID identification number(s) for the author(s) of this article can be found under https://doi.org/10.1002/adma.202419088

DOI: 10.1002/adma.202419088

with greater permittivity and similarly negatively charged surfaces could prove even more useful in increasing the energy density of PVDF capacitors.

MXenes are a family of 2D transition metal carbides, nitrides, and carbonitrides that have attracted significant attention in recent years due to their unique electronic, chemical, and optical properties. These nanomaterials have a general formula of $M_{n+1}X_nT_x$ with n ranging from 1 to 4, where M is a transition metal (Ti, V, Nb, etc.), X is C and/or N, and T_x represents a variety of surface terminations, commonly ═O, —OH, —F, and —Cl.[14] These mixed surface terminations arise from the synthesis of MXene by etching away A-element layers from the MAX phase precursor using a mix of HF and HCl acids, resulting in hydrophilic nanosheets that are easily dispersed in aqueous solutions.[14] Alternative synthesis methods, such as molten salt etching, can produce MXenes with uniform halogen surface terminations[15] but will likely require more dedicated research to reach the scale of mixed acid etching. Challenges such as dispersibility and interfacial compatibility persist with many MXene composites, hindering further progress in creating high-performance materials. Hydrophobic polymers show poor compatibility with hydrophilic MXenes,[16,17] limiting the selection of composite systems. Given PVDF's hydrophobicity, compatibility issues lead to MXene agglomeration, non-uniformity of dispersion, and overall decreased functionality in the composite. Limited research has been done in the field of MXene-PVDF composites for thin-film dielectric capacitors, and results thus far have not been as impressive as with other 2D materials. Li et al.[18] fabricated heterostructures of $Ti_3C_2T_x$ MXene and PVDF with layer-by-layer assembly to improve dielectric permittivity while minimizing the loss tangent but achieved a maximum energy density of only 7.4 J cm^{-3} and a corresponding efficiency of 76%. Feng et al.[19] designed an alternative "gradient sandwich" heterostructure that led to higher breakdown voltage in the film, but still resulted in an energy density of only 12.5 J cm^{-3} and discharge efficiency of 60%. To effectively utilize MXene in PVDF composites for this application, lower loadings of nanomaterial are necessary to avoid percolation and leakage current that can greatly decrease the breakdown voltage. This can be difficult to accomplish, given that poor dispersions of MXene in the hydrophobic matrix and weak interfacial interactions can limit the functionality of lower-loading composites. Furthermore, most means of blending this nanomaterial with polymers can affect the functionality of the MXene itself.

MXenes are typically blended with polymers through a solvent exchange process, commonly involving centrifugation or filtration of the nanomaterial out of water and replacement with the alternative solvent.[17,20] Dispersion in the solvent is most often done by bath or probe ultrasonication. Unfortunately, sonication is an aggressive, high-power process that can diminish flake size and introduce defects, proving detrimental to MXene properties such as conductivity or permittivity.[21] Other methods that involve post-processing or interfacial agents can be time-intensive and affect MXene or overall composite properties.[17,22]

This work introduces a soft delamination method for dispersing MXene into organic solvents without sacrificing flake size or quality. The PC solvent selection not only provides an excellent suspension for stable solutions of MXene but also results in nearly pure β-phase PVDF with enhanced permittivity due to polar interactions during film casting.[7] Porous PVDF-MXene films fabricated through a NIPS process have demonstrated exceptional energy density and record discharge efficiency when examined in dielectric capacitors. $Ti_3C_2T_x$ with mixed terminations has been compared to chlorine-terminated $Ti_3C_2Cl_2$ made through molten salt synthesis. Porous composite films produced in this work significantly outperformed similarly made dense films and resulted in remarkably high efficiency due to the enhanced dielectric permittivity from MXene and structural control from composite processing. Thin-film capacitors made using this method offer a solution to energy storage applications in the next generation of electronics.

2. Results and Discussion

2.1. MXene Synthesis and Delamination

X-ray diffraction (XRD) patterns of the unetched Ti_3AlC_2 MAX phase compared to that of the etched $Ti_3C_2T_x$ MXene delaminated in PC are shown in Figure S1a,b (Supporting Information). Indexed peaks for the MAX phase confirm Ti_3AlC_2 structure with a (002) peak at 9.40°, corresponding to a *d*-spacing of 9.4 Å. This peak shifts to 6.68° in the delaminated MXene, indicating an increase in *d*-spacing to 13.2 Å, a typical value for this MXene that correlates with literature.[14,23] Scanning electron microscopy (SEM) confirmed the etching of the A layer from the MAX phase, as seen in the difference between **Figure 1c,d**. The multilayer $Ti_3C_2T_x$ showed the familiar accordion-like structure, which can be delaminated by sonication,[21,24] high-shear processing,[25,26] or chemical intercalation and mechanical agitation. The latter process has been shown to produce larger flakes,[23,27] which can lead to increased dielectric permittivity in the composite due to the accumulation of charges at the interfaces.[28] To maximize energy density in the PVDF-MXene systems, a softer delamination was performed to disperse single-layer $Ti_3C_2T_x$ directly into PC without the need for sonication or excess agitation from solvent exchange. Dispersion of MXene in PC improves polymer compatibility and provides additional benefits such as MXene stability (elimination of oxidation or hydrolysis during storage).[20,29] For polymer compatibility, PC has the advantage of not only being green and sustainable compared to many commonly used solvents for PVDF,[9,30] but also facilitating the formation of PVDF's β-phase due to high polarity and solvent interactions.[7] The PC-delaminated $Ti_3C_2T_x$ is of higher quality compared to other attempts to disperse MXene into organic solvents[20,29]

The standard process for delaminating multilayer $Ti_3C_2T_x$ aqueously was slightly adjusted for this work. LiCl was still used as the intercalating agent to swell the layered MXene, and residual salts were washed from the solution with deionized (DI) water. The key difference was redispersing the swollen MXene in PC immediately before the bulk of delamination began. Results can vary, but delamination tends to occur after 1–2 washes with DI water due to the agitation from shaking to redisperse the MXene.[23] Sedimented $Ti_3C_2T_x$ was redispersed in PC after the second wash with DI water, which required ≈ 10 min of mechanical agitation via a paint shaker before

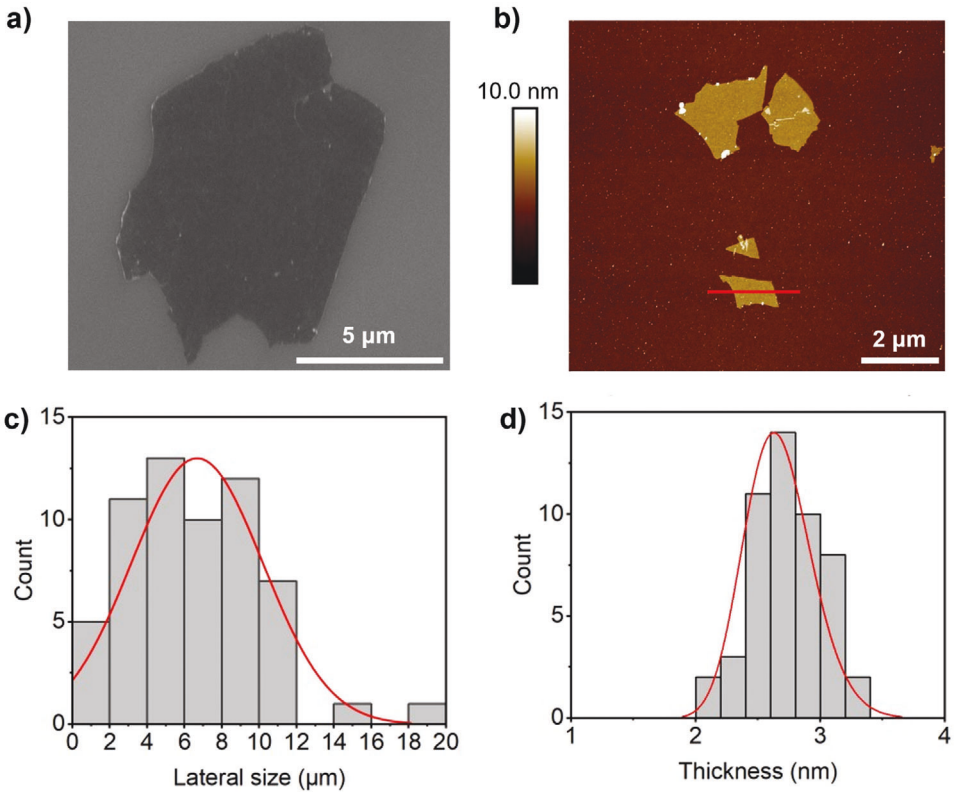

Figure 1. a) SEM image of larger $Ti_3C_2T_x$ flake, b) AFM image of several $Ti_3C_2T_x$ flakes, c) lateral size distribution of a sample of 60 flakes of $Ti_3C_2T_x$ delaminated in PC, obtained by analyzing AFM and SEM images and d) thickness distribution of a sample of 50 flakes of $Ti_3C_2T_x$ delaminated in PC, measured with AFM.

further centrifugation. The supernatant of PC and water were separated and subsequent redispersions in PC were done by gentle hand shaking, minimizing damage and size reduction of MXene flakes. The yield from this delamination was comparable to that from standard aqueous delamination, and flake size was determined by SEM and atomic force microscopy (AFM), as seen in Figure 1. SEM (Figure 1a) and AFM (Figure 1b) imaging show flake morphology as well as larger and smaller flakes. A sample of 60 flakes from both SEM and AFM imaging were measured laterally and found to be almost entirely >1 μm flakes with an average flake size of ≈7 μm (Figure 1c) and an average thickness of ≈ 2.6 nm (Figure 1d). This is slightly thicker than the reported $Ti_3C_2T_x$ monolayers with 1–2 nm thickness,[31] confirming that single-layer flakes likely have residual PC on the surface and/or interface between the MXene and substrate. Given the typical *d*-spacing seen in vacuum-filtered films, this residual PC can be removed through filtration or washing. The average lateral size of 7 μm exceeds that of typical MXenes dispersed through ultrasonication, which are often submicron size.[21]

Hydrophobic, pure chlorine-terminated $Ti_3C_2Cl_2$ MXene was synthesized by a previously reported Lewis acid molten salt etching method with $ZnCl_2$ and delaminated by Li-ion intercalation in organic solvents and bath sonication.[15] This process yielded smaller flakes that dispersed easily into various organic solvents such as PC. MXene flakes had typical lateral sizes between 1–2 μm, as shown in Figure S2a,b (Supporting Information). Raman spectra of synthesized $Ti_3C_2Cl_2$ and $Ti_3C_2T_x$ both show the presence of characteristic MXene peaks confirming successfully synthesized structures (Figure S2c, Supporting Information).[15] The conductivity of pure $Ti_3C_2Cl_2$ films was measured to be ≈8000 S cm^{-1}, comparable to typical $Ti_3C_2T_x$ MXene.[14] One sample each of porous and nonporous composite film with $Ti_3C_2T_x$ was fabricated for this study. The pure chlorine terminations on the surface of these flakes should facilitate stronger interfacial interactions with the hydrogen groups on the backbone of PVDF chains.[32] PVDF's *β*-phase is unique in that the hydrogen groups are all present on only one side of the polymer chain, with the fluorine groups polarized to the other side due to the repeating trans bonds in *β*-phase chains and lack of gauche bonds.[33] Figure S3 (Supporting Information) shows a schematic of PVDF crystalline structures (Figure S3a, Supporting Information) and the bonding between polymer chains and MXene surfaces (Figure S3b, Supporting Information). Strong dipole and electrostatic interactions can occur between these chains and the negatively charged surface groups of MXene sheets. Still, this effect can be enhanced when the sheets contain pure chlorine terminations compared to mixed terminations due to the increased density of highly electronegative elements.[32] By integrating MXenes with carefully selected chemistry into PVDF composites, nucleation and alignment of the *β*-phase (Figure S3c, Supporting Information) can be improved to greatly enhance dielectric properties.

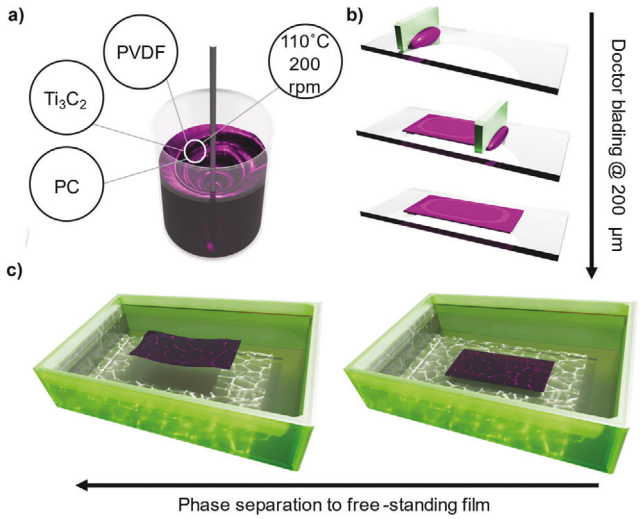

Figure 2. Schematic of NIPS process for preparing PVDF-MXene composite membranes. a) Blending of PVDF and MXene by heated dissolution into propylene carbonate suspension of $Ti_3C_2T_x$, b) doctor blading of polymer solution onto a glass substrate, and c) submersion in a non-solvent bath of DI water.

2.2. PVDF-MXene Composite Processing and Characterization

Porous composites of MXene and PVDF polymer were produced through a NIPS process, commonly used for polymer membrane preparation,[9,34,35] as shown schematically in **Figure 2**. This process involves formulating a dope solution of dissolved polymer in an organic solvent, in this case, PVDF in PC, with the addition of MXene, as seen in Figure 2a. Blade coating the dope solution (Figure 2b) allows for control of film thickness and aids in orienting MXene flakes and PVDF chains through induced shear stress.[36–38] Through submersion in a non-solvent bath of DI water (Figure 2c), two distinct phases of the solution emerge: a polymer-rich phase that sets into a free-standing film and a solvent-rich phase that leaches out of the film, forming a porous network as it does.[9] This process has the advantage of scalability and adaptability, with parameters such as temperature, bath composition, and solids content easily altered to change membrane structure and properties. Dense, non-porous composites were fabricated using the same method, but with an additional heating step before submersion to allow for slow evaporation of most of the residual solvent before fully setting the film.

Using measured concentrations of $Ti_3C_2T_x$ in PC, four porous samples of pristine PVDF, 0.1 wt.%, 1 wt.%, and 3 wt.% MXene were produced, denoted as P_PVDF, P_X_0.1, P_X_1, and P_X_3, respectively. Samples were named for whether they are porous (P) or non-porous (N), the termination group of the MXene filler (X for mixed terminations and Cl for pure chlorine terminations), and the content of the MXene filler by mass loading. For comparison, a small amount of $Ti_3C_2Cl_2$ MXene was dispersed in a porous film at 0.5 wt.%, denoted as P_Cl_0.5. Dense, non-porous films of pristine PVDF and $Ti_3C_2Cl_2$ were fabricated as well, denoted as N_PVDF and N_Cl_0.5, respectively. Table S1 (Supporting Information) details the structure, MXene surface terminations, and MXene mass and volume loading for each uniquely named sample.

XRD (**Figure 3a**) shows the presence of a notable peak around 20.26° across all porous films. This peak is associated with the β-phase of PVDF, compared to two distinct 19.9° and 26.56° peaks for the α-phase and a shoulder peak around 18.5° for both the α- and γ-phases.[33,39] The dominance of the β-phase peak and lack of any other peaks in that area indicate that these PVDF films all exhibit ≈ 100% β-phase in their crystalline portions. This is due to strong interactions between the polymer and highly polar solvent, facilitating the formation of polar β-phase spherulites within the solution.[7] The 002 peak from MXene around 6.7° is broad and has a lower intensity in higher loading samples, indicating that there may be some small agglomerations present within the composite despite a mostly spread out distribution of flakes.

The Raman spectra (Figure 3b) confirm the presence of the β-phase peak at 840 cm^{-1} and the lack of α-phase peaks at 795 cm^{-1} in both P_PVDF and P_X_3 (background removal applied). Additionally, characteristic PVDF peaks for CH_2 twisting, scissoring, and stretching modes are observed at 1430 and 2900 cm^{-1} in both pure PVDF and composite samples in the full unprocessed Raman spectra (Figure S4, Supporting Information).[40] The $Ti_3C_2T_x$ delaminated in PC was also examined under Raman to confirm peaks are analogous to MXene delaminated in water.[41] These same peaks are present in the spectrum of P_X_3, denoting no chemical changes to the MXene during PC delamination or composite processing through NIPS. The peaks with the largest intensities corresponding to E_g (Ti, C, T_x) and $A_{1\,g}$ (C) modes remain at the same wavenumbers in the PC-delaminated sample, indicating comparable surface terminations.[42] FTIR full spectra (Figure 3c) and normalized spectra in the area of interest (Figure 3d) confirm the crystalline structure with the presence of β-phase peaks at 1275 and 840 cm^{-1} and lack of notable peaks for α-phase at 765 cm^{-1} or γ-phase at 1233 cm^{-1}.[39] The full spectra show the IR shielding behavior reported for MXenes,[43] as the relative intensity of each sample examined under identical conditions decreases with increased MXene loading. This shielding behavior in such low-loading composites could prove promising for other applications, such as thermal management or heat dissipation within electronic devices.[44]

Figure 4a shows the surface of porous pristine PVDF with a spherulitic structure that forms porous networks. The addition of hydrophilic $Ti_3C_2T_x$ MXene facilitated the formation of a tighter pore structure and skin-like surface for the composite films due to enhanced compatibility with the non-solvent and a more rapid mass-exchange rate.[45] Figure 4b shows the effect of just 1 wt.% inclusion of hydrophilic MXene, leading to faster phase separation and a network of micro- and macrovoids rather than a more open network of slow-forming spherulites. There may be solubility parameters affecting these structures as well, as the MXene may adsorb or attract PC on the surface of flakes, and higher loadings within the dope solution can reduce the available solvent for the dissolution of PVDF. Thus, a higher solids content in the dope can cause faster phase separation and the formation of a more defined pore structure, forming a stronger and more selective membrane.[9,34,45] This effect can be seen in the higher-loading porous composite P_X_3 in Figure 4c with an even tighter and more defined pore structure. An angled

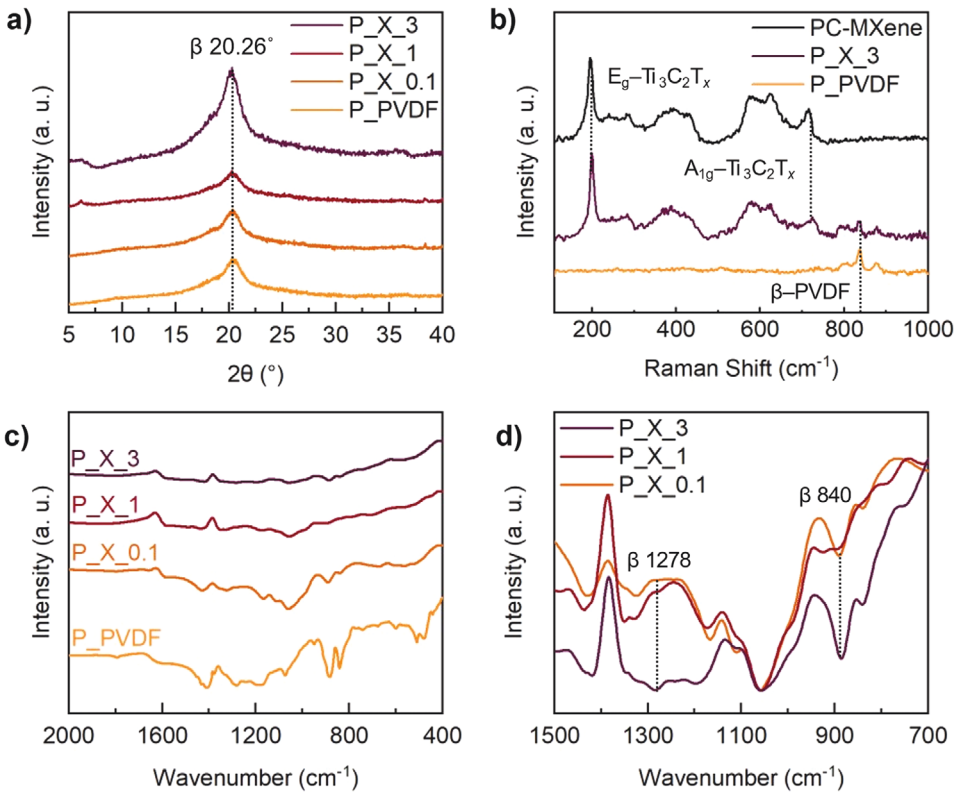

Figure 3. a) XRD of porous PVDF-MXene samples, b) Raman spectra of porous pristine PVDF, porous 3 wt.% $Ti_3C_2T_x$ in PVDF, and PC-delaminated $Ti_3C_2T_x$, c) full FTIR spectra of porous PVDF-MXene samples and d) normalized FTIR spectra for porous PVDF-MXene samples at the region of interest for PVDF characterization.

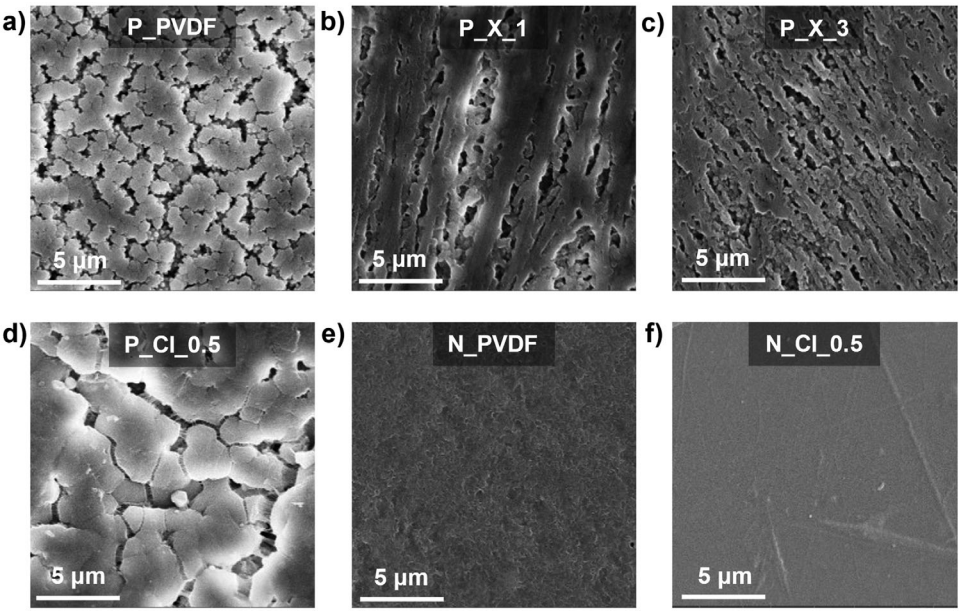

Figure 4. SEM images of the surfaces of a) porous pristine PVDF, b) 1 wt.% $Ti_3C_2T_x$ in porous PVDF, c) 3 wt.% $Ti_3C_2T_x$ in porous PVDF, d) 0.5 wt.% $Ti_3C_2Cl_2$ in porous PVDF, e) non-porous pristine PVDF, f) 0.5 wt.% $Ti_3C_2T_x$ in non-porous PVDF.

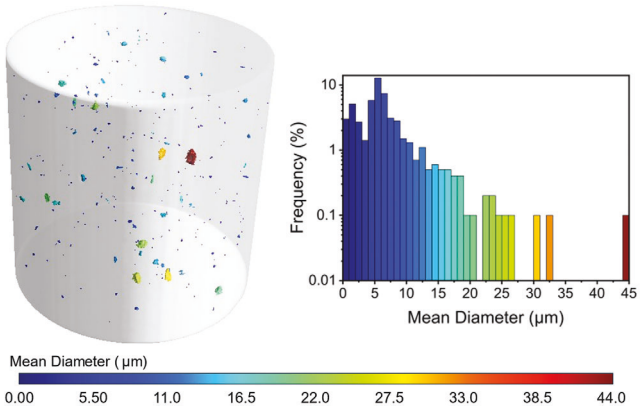

Figure 5. NanoCT analysis of 1 wt.% $Ti_3C_2T_x$ in porous PVDF showing the distribution of MXene within a 0.166 mm^3 field of view. The histogram plots the distribution of flake and/or agglomeration sizes.

cross-section of this sample taken by FIB-SEM can be seen in Figure S5a (Supporting Information), revealing many closed microvoids throughout the film. These voids may also aid in enhancing dielectric properties through increased permittivity and interfacial polarization. Including a small amount of hydrophobic MXene appears to lead to the formation of larger spherulites seen in Figure 4d, likely due to a slower phase separation rate. A more hydrophobic solution has poor compatibility with the non-solvent, leading to a slower mass-exchange rate and slow nucleation of larger, independent spherulites.[45] The phase separation rate can be partially elucidated from the time between non-solvent immersion and complete separation of the free-standing film from the substrate, which decreased from ≈90 s in pristine PVDF samples to ≈35 s with the inclusion of only 3 wt.% $Ti_3C_2T_x$. The inclusion of 0.5 wt.% $Ti_3C_2Cl_2$ had a less pronounced effect, with separation from the substrate occurring ≈ 95 s. These trends may not directly quantify phase separation kinetics, but do bolster the claim that the rate of separation varies with MXene content and surface terminations. Morphology differences can also be seen between Figure 4e (N_PVDF) and 4f (N_Cl_0.5). The surface of nonporous pristine PVDF was still rough, with many divots and partial micropores forming due to the phase separation at higher temperatures and during final immersion in the non-solvent bath. The surface of nonporous PVDF with hydrophobic MXene integrated into the matrix was much smoother due to slower phase separation kinetics, leading to a more uniform polymer structure.

Further structural analysis of composites was performed by micro-computed tomography (Micro-CT), which enables non-destructive visualization of the internal structure of the sample in 3D. This comprehensive understanding allows for a deeper exploration of how microstructure influences the functionality and performance of the composites. **Figure 5** displays ≈0.166 mm^3 field of view for P_X_1 scanned with Micro-CT, yielding valuable insights into the quality of discussed samples. The higher X-ray absorption of the MXene enables a clear contrast between the nanofiller and the polymer matrix in Micro-CT. This contrast is crucial for distinguishing the two phases in the composite structure. The mean diameter of flakes and aggregations were plotted in a histogram, showing ≈ 99% of particulates smaller than 20 μm, roughly the largest single flake size seen in AFM and SEM. The nanofillers exhibit homogeneous dispersion within the polymer matrix with minimal agglomeration. These agglomerations likely occurred while the MXene was stored in a liquid solvent, as a larger agglomeration of several flakes can be seen in the SEM of flakes deposited directly from the solution (Figure S5b, Supporting Information). Despite the agglomerations appearing in this matrix being relatively small and infrequent, their presence highlights the importance of utilizing MXene shortly after synthesis and delamination to minimize restacking and oxidation. The effective dispersion of MXene flakes through the PVDF matrix aids in reducing leakage current from large agglomerations and percolative networks, enhancing dielectric properties.

2.3. Thin-Film Capacitor Testing

The cross-sectional SEM images of the free-standing PVDF-MXene composite films show an average thickness between 5.79 and 7.31 μm (Figure S5d, Supporting Information), with an average thickness of 6.5 μm considered in all the following measurements for capacitor performance. Capacitors were fabricated using silver as the top and bottom plate, as shown in Figure S5e,f (Supporting Information). The area of each fabricated capacitor was calculated to be ≈400000 μm^2, measured using an optical microscope. Thin Au wires of 0.025 mm diameter were used to connect the metal capacitor plates to the ferroelectric testing setup. Some samples, including non-porous composites of $Ti_3C_2T_x$, were excluded from testing in capacitor applications due to excessive leakage as the conductivity increased with higher loading. P_X_0.1 was excluded as no significant change was observed in electric conductivity or dielectric behavior compared to pristine PVDF.

The polarization versus electric field (*P-E*) loops for N_ PVDF and N_Cl_0.5 are shown in Figure S6 (Supporting Information). Polarization and energy density of several capacitors were measured, and the P-E loops for the three highest performance samples, C_1, C_2, and C_3, are plotted. Nonporous pristine PVDF exhibited maximum polarization of 21.2±1.5 μC cm^{-2} for capacitors C_1, C_2, and C_3, respectively (Figure S6a, Supporting Information), while the corresponding value for nonporous PVDF with 0.5 wt.% $Ti_3C_2Cl_2$ was 19.2±1.7 μC cm^{-2} (Figure S6b, Supporting Information). The polarization values of pristine PVDF were more consistent than those of the PVDF-MXene composite film. The variation of polarization of composite samples could be due to the nonuniformity of the MXene distribution in the polymer matrix or variations in flake size and morphology, as the current delamination method for molten salt-etched MXenes produces solutions that contain both single-layer and few-layer MXene.[15]

Figure S6c,d (Supporting Information) displays the discharge energy density (U_d) extracted from the polarization measurements and efficiency (η) extracted from the discharge and charge energy density plotted as a function of applied electric field for N_PVDF and N_Cl_0.5, respectively. The discharge energy density of N_PVDF at 250 MV m^{-1} was 18 J cm^{-3}, whereas the energy density for N_Cl_0.5 was 22 J cm^{-3} at 290 MV m^{-1}. The efficiency also increased in the composite sample compared to pristine PVDF from 79% to 85% at the average maximum applied electric field. The composite samples showed slightly less

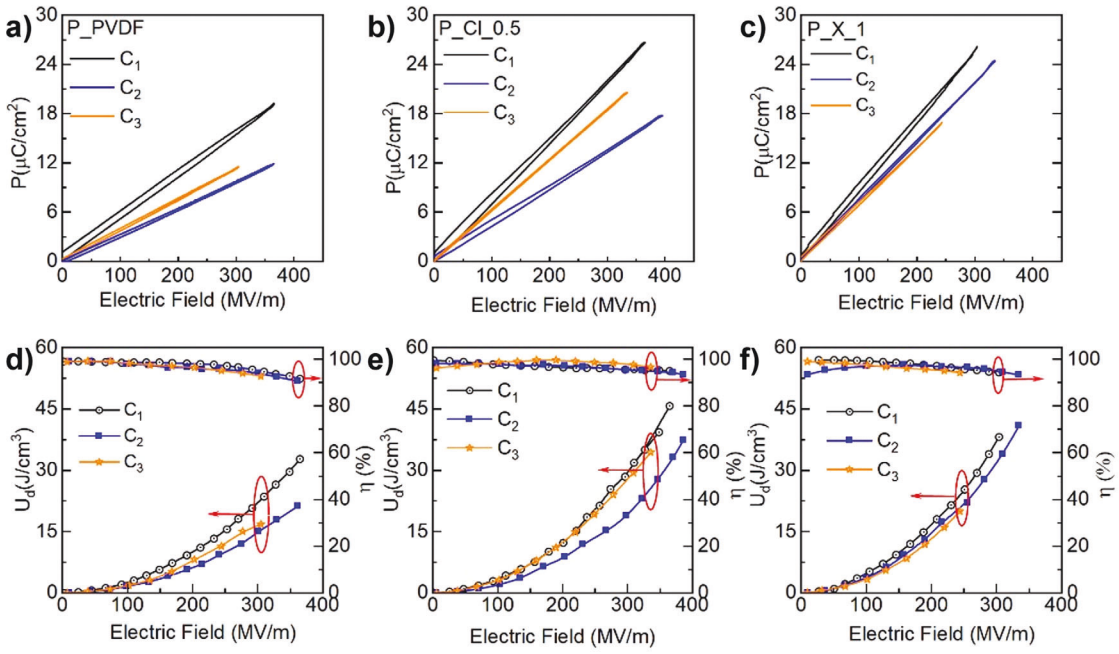

Figure 6. a–c) *P-E* loops of the three best-performing capacitors (C_1, C_2, and C_3) for porous pristine PVDF, 0.5 wt.% $Ti_3C_2Cl_2$ in porous PVDF, and 1 wt.% $Ti_3C_2T_x$ in porous PVDF, d–f) corresponding energy density and efficiency curves for these porous PVDF-MXene films.

hysteresis loss than pristine PVDF capacitors, as shown in Figure S6c (Supporting Information). There has been limited research to date on the capacitive energy storage of polymer/MXene composites. Still, the energy density values reported for these nonporous samples are notably higher than the reported values of PVDF-MXene capacitors.[18,19,46] This is likely due to the content of β-phase within the PVDF films, greatly enhancing the dielectric constant. As seen in Figure S7 (Supporting Information), the dielectric constant of the pristine PVDF is already at the higher end of reported values[46,47] with a constant of ≈19 at 10 kHz. The corresponding dielectric loss in the nonporous PVDF (Figure S7c, Supporting Information) was notably low, with a value of 0.017 at 10 kHz. Figure S7b (Supporting Information) shows the enhanced dielectric constant of nonporous PVDF with the addition of 0.5 wt.% $Ti_3C_2Cl_2$, reaching a value of ≈27 at 10 kHz while still maintaining a low loss tangent of only 0.02 (Figure S7d, Supporting Information). The measured dielectric constant and loss curves were notably more consistent in pristine PVDF than in the composite film. This results from much more uniformity throughout the film in pristine samples, while the composite samples showed a small degree of inconsistency due to the dispersed nanofiller. Additionally, the slow formation of larger spherulites of β-phase PVDF surrounded by more insulating amorphous polymer likely led to greatly enhanced dielectric properties with incredibly low loss tangents, providing an ideal system for dielectric charge storage.

Porous composites of PVDF and MXene yielded better results than nonporous ones, with geometry and measurement parameters between the sample sets being nearly identical. **Figure 6a–c** depicts the P-E loops of three capacitor sample sets: porous pristine PVDF, 0.5 wt.% $Ti_3C_2Cl_2$ in porous PVDF, and 1 wt.% $Ti_3C_2T_x$ in porous PVDF. P_PVDF showed a maximum polarization of 14.2±3.5 μC cm^{-2}, increasing to 21.6±3.7 μC cm^{-2} for P_Cl_0.5. P_X_1 had polarization of 22.5±4.0 μC cm^{-2}, as shown in Figure 6c. These results show that the MXene-incorporated porous PVDF nanocomposites had higher polarization values than porous pristine PVDF and PVDF composite systems seen in the literature.[48] The dielectric constant for porous pristine PVDF increased only slightly from its nonporous counterpart, from 19 to ≈20 at 10 kHz (Figure S8a, Supporting Information), but with a nearly identical loss tangent of 0.017 (Figure S8d, Supporting Information). These values are very impressive for pristine PVDF due to the contributions of the highly polar β-phase. The alignment of β-phase chains amplifies dielectric permittivity by increasing dipole density throughout the thickness of the film. Porous PVDF with 0.5 wt.% $Ti_3C_2Cl_2$ showed a more significant improvement from the nonporous films, with the dielectric constant increasing from 27 to ≈31 (Figure S8b, Supporting Information) while maintaining a lower loss tangent of 0.017 at 10 kHz (Figure S8e, Supporting Information). Porous PVDF with 1 wt.% $Ti_3C_2T_x$ showed the highest dielectric constant of all measured samples with a value of ≈45 at 10 kHz (Figure S8c, Supporting Information), likely due to the increased conductivity and larger lateral size of the flakes. However, dielectric loss in these samples remained even lower than the nonporous composite sample, at a value of 0.019 at 10 kHz Figure S8f, Supporting Information). The dielectric properties of these porous PVDF composites are impressive when compared to literature data,[47] and their extremely low loss is an important contributing factor to the efficiency and performance of fabricated capacitors. Porous materials often show both lower dielectric constant and loss due to the presence of low-permittivity air gaps in the matrix.[49,50] However, the faster phase separation from immediate non-solvent immersion likely led to increased nucleation of the β-phase, while

the porous structure minimized charge conduction and energy dissipation. Pores in the composite introduce heterogeneous dielectric regions (PVDF/air), creating local electric field gradients. These gradients induce interfacial polarization, particularly at low frequencies, where charges have sufficient time to align at the interfaces. The porous structure increases the effective dielectric constant of the composite by adding additional polarization mechanisms not present in dense films.

A noteworthy feature observed from these results was extremely low hysteresis loss compared to the nonporous PVDF capacitors shown in Figure S6 (Supporting Information). The low hysteresis in porous capacitor samples contributes to the significantly enhanced energy density. The porous matrix has the advantage of high surface area created by the network of pores, allowing for the trapping of charges at polymer-MXene and polymer-air interfaces, as well as isolation of ferroelectric β-phase domains to reduce energy dissipation from domain switching. The enhanced interfacial polarization in porous films, which dominates the dielectric response at lower electric fields, contributes to the observed linearity in P-E loops, and the porous architecture minimizes cooperative interactions between ferroelectric domains to reduce hysteresis.[19] These factors all lead to increased energy storage capacity compared to nonporous materials. Nanoporous materials are advantageous for electrochemical capacitor systems, owing to the enhanced ion transport in smaller, disordered domains and larger surface area for charge storage,[51,52] but similar materials have been less explored for dielectric applications. The porosity and increased disorder within these samples may also aid in providing more separation between conductive nanofillers, allowing for higher loading of nanofillers without excessive leakage current.

The extracted energy density for the P_PVDF, P_Cl_0.5, and P_X_1 are displayed in Figure 6d–f. The highest discharge energy density of 32 J cm^{-3} at 365 MV m^{-1} was measured for the porous PVDF capacitor (Figure 6d). The 0.5 wt.% MXene incorporated porous PVDF capacitors show a significantly enhanced energy density of 46 J cm^{-3} (Figure 6e) compared to the pure porous PVDF. Similar energy density was measured at ≈45 J cm^{-3} for 1 wt.% $Ti_3C_2T_x$ in porous PVDF and shown in Figure 6f. These values are significantly higher than reported polymer-based nanocomposites containing MXene nanofiller.

Feng et al.[19] reported energy density of 12.5 J cm^{-3} with a gradient sandwich-structured MXene/PVDF composite where three layers of PVDF blended with varying concentrations of $Ti_3C_2T_x$ MXene were stacked on top of each other for a thicker composite film. Each layer acted as a different material with varying dielectric permittivity, providing higher interface polarization to enhance the capacitive energy density. In the PVDF/MXene composites presented in this work, the mixture of MXene in porous PVDF media acts as a single-layer homogenous system to enhance the energy density. The porous polymer matrix shows ultra-low hysteresis loss, which is the key to improved energy density and record efficiency. The incorporation of MXene as a filler further enhanced the energy density without increasing any dielectric loss. These results demonstrate that the careful design of composite structures with MXene filler can significantly enhance both breakdown strength and energy storage capabilities. These homogenous systems could be integrated into heterostructures for even higher-performance capacitors. In another report, Wang et al.[46] demonstrated a hybrid material system of MoS_2@MXene/PVDF to achieve a high breakdown strength of 424.11 MV m^{-1} and a discharged energy density of 17.22 J cm^{-3} with 3.47 wt.% MoS_2@MXene, which represents a 350% increase of energy density over pure PVDF. The energy density values of these films, especially the porous composites, are exceptionally high compared to previous MXene-PVDF systems studied. The high experimental values obtained for energy density can be attributed to many factors, including the testing of composites at lower frequencies (25 Hz on a Radiant Ferroelectric tester), allowing for higher dielectric permittivity, and the nonlinear dielectric behavior of polymers like PVDF at higher strength electric fields.[53] Binary systems of PVDF and MXene presented in this work can act as the foundation for more complex composites that outperform the existing capacitors.

The breakdown strength for each set of samples was measured by increasing the applied voltage on each capacitor and measuring the polarization or current on the sample. The breakdown strength is the minimum voltage that causes a portion of a dielectric film to experience electrical breakdown and become electrically conductive. The Weibull probability distribution predicts the probability of failure and was plotted as a function of the applied electric field where the breakdown occurs, presented in **Figure 7**. The data points represent the experimental measured values, and the solid line shows the Weibull probability fit using (Equation 1):

$$P\ (E) = 1 - \exp\left(-\left(\frac{E}{E_{BD}}\right)^{\beta}\right) \quad (1)$$

where P is the cumulative probability of failure, E is the electric field at dielectric failure, E_{BD} is the dielectric breakdown field strength (the dielectric strength at 63.2% probability of failure), and β is a shape parameter that defines the film uniformity across the sample. Higher β values correspond to higher-quality samples for dielectric capacitors. Figure 7a shows the Weibull plot of the nonporous PVDF capacitor (blue circles) and the nonporous composite of $Ti_3C_2Cl_2$ (orange triangles). N_PVDF has a breakdown strength of E_{BD} = 250 MV m^{-1} with a β value of 12.4, showing uniform film quality or reliability of the film. The breakdown strength increased to 342 MV m^{-1} for N_Cl_0.5 with a β value of 7. The lower β value in the composite capacitor suggests less uniformity throughout the film, likely due to the low mass loading of the nanofiller and the variability in flake size and thickness. Figure 7b depicts the probability of failure as a function of the applied electric field for P_PVDF (blue circle), P_Cl_0.5 (orange triangular), and P_X_1 (green rectangular) composites. The solid lines are the Weibull fit to extract the breakdown strength of the sample. The porous pristine PVDF samples had a breakdown strength of E_{BD} = 380 MV m^{-1} with shape parameter β value of 15 which was much higher than the breakdown strength and β value obtained from the nonporous PVDF sample. The immediate phase separation involved in producing the porous samples may lead to more uniform films due to faster solidification through the entire thickness of the polymer as it sets. The porous PVDF with 0.5% $Ti_3C_2Cl_2$ achieved an even higher breakdown strength of E_{BD} = 406 MV m^{-1} with excellent reliability of β = 13. This suggests that the conductive MXene nanofiller can

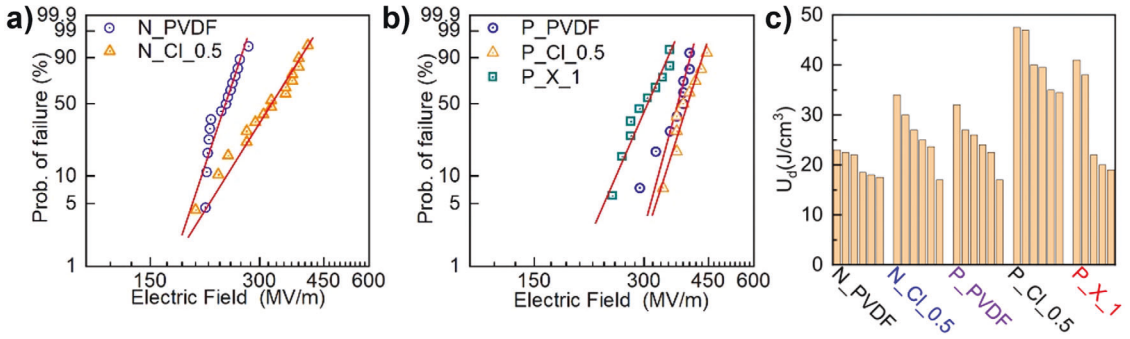

Figure 7. a) Weibull probability distribution plots for nonporous pristine PVDF and 0.5 wt.% $Ti_3C_2Cl_2$ in nonporous PVDF, b) Weibull plots for porous pristine PVDF, 0.5 wt.% $Ti_3C_2Cl_2$ in porous PVDF, and 1 wt.% $Ti_3C_2T_x$ in porous PVDF, c) histogram of energy density for all measured capacitors across the five compositions as indicated under each set of data.

increase the breakdown voltage of polymer samples at lower loading. This could be due to excellent interfacial interactions with the chlorine-terminated surfaces of these MXenes. Such interfacial compatibility can lead to a tighter packing of the polymer around the nanofiller, causing a shielding effect that slows the transport of electrons.[32] The leakage current of both P_PVDF and P_Cl_0.5 can be analyzed from current versus voltage measurements in Figure S9a,b (Supporting Information). The leakage current remained very low (<0.2 nA) until the point of electrical breakdown. This is a crucial aspect of high-performance dielectric capacitors and minimizes energy loss during charging and discharging. P_X_1 exhibited a lower breakdown strength of E_{BD} = 320 MV m^{-1}, highlighting the more direct effect on film conductivity that mixed termination MXenes can have. The low mass loading of 1 wt.% $Ti_3C_2T_x$ caused an increase in electrical conductivity and leakage current, slightly decreasing the breakdown strength of the film. However, the energy density was similar to the 0.5 wt.% $Ti_3C_2Cl_2$ composite due to the enhanced dielectric strength and interfacial polarization between the higher content of MXene fillers and polymer matrix.

Figure 7c presents the histogram plot of all measured capacitors across the five compositions N_PVDF, N_Cl_0.5, P_PVDF, P_Cl_0.5, and P_X_1, providing a comprehensive comparison of energy density variations. The data confirms that the porous PVDF with 0.5% $Ti_3C_2Cl_2$ consistently outperformed other compositions in terms of both energy density and efficiency, while samples with 1 wt.% $Ti_3C_2T_x$ showed more variability, possibly due to variations in flake size and small agglomerations forming within the matrix. Further exploration into various compositions under 1 wt.% loading of mixed termination MXenes could yield more promising results by reducing the impact on the breakdown voltage. Utilizing processing methods to produce porous composites of PVDF and various chemistries of MXene appears to be an auspicious path toward fabricating a new generation of ultra-high-performance capacitors.

Compared to similar composite systems that have integrated 2D nanofillers into dielectric polymer capacitors, this work presents PVDF thin films showing higher energy density and efficiency, as seen in the Ashby plots in **Figure 8**. The NIPS process for integrating both PC-delaminated $Ti_3C_2T_x$ and pure chlorine terminated $Ti_3C_2Cl_2$ has produced capacitors that outperform similar polymer systems with nanofiller of mica,[54–56] $Ca_2Nb_3O_{10}$,[57,58,13] boron nitride nanosheets,[59–66,12,67–70] MoS_2,[46,71–73] and $Ti_3C_2T_x$ MXene.[18,19,46,74] This work demonstrates that energy density and efficiency can be significantly improved even without substantial enhancement of the breakdown voltage of the polymer film. Considering dozens of MXenes available and a variety of surface terminations, exploration of a wider range of compositions and chemistries should allow one to determine trends in this area and further improve the performance. Incorporation of these composites

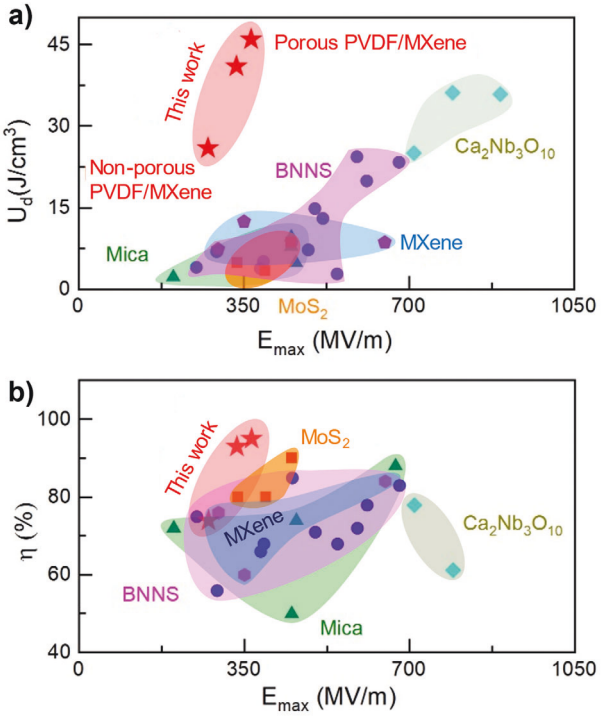

Figure 8. Ashby plots compiled from the literature on enhancing PVDF a) dielectric energy density and b) discharge efficiency through composite structures with 2D nanofillers: mica, boron nitride nanosheets (BNNS), $Ca_2Nb_3O_{10}$, MoS_2, previous work with $Ti_3C_2T_x$ MXene, compared to the results from this work.

into heterostructures and more complex systems may be the key to the future of dielectric capacitors.

3. Conclusion

This study presents a method for producing high-performance PVDF/MXene composites with improved dielectric properties at low loadings of MXene. Soft delamination of multilayer MXene directly into a green solvent such as propylene carbonate yields stable colloidal solutions of large MXene flakes with enhanced compatibility with PVDF. The combination of a polar PC solvent and 2D MXene nanofiller facilitates the formation and alignment of pure β-phase crystalline structure, greatly enhancing dielectric properties. The NIPS process for fabricating polymer membranes is highly advantageous for composite processing due to adaptability and scalability. This process can produce dense and porous films, the latter showing promising results as thin film capacitors. Incorporating MXene into nonporous and porous PVDF films significantly enhances the dielectric and energy storage properties. The addition of only 0.5 wt.% $Ti_3C_2Cl_2$ MXene, especially in porous PVDF, resulted in a higher energy density, improved efficiency, and increased breakdown strength compared to pure PVDF and higher MXene-loaded samples. The optimal combination of low MXene content with excellent interfacial compatibility and porosity of the polymer led to the best performance, achieving an energy density of 46 J cm^{-1} and a breakdown strength of 406 MV m^{-1}. Higher loading of mixed acid-etched $Ti_3C_2T_x$ MXene content at 1 wt.% led to reduced breakdown voltage but comparable overall performance. These findings underscore the importance of careful control of MXene content and structural design to maximize the potential of PVDF-based dielectric capacitors for high-performance energy storage.

4. Experimental Section

Synthesis of $Ti_3C_2T_x$ MXene: MXene $Ti_3C_2T_x$ was synthesized by selective wet-chemical etching of Al from MAX phase Ti_3AlC_2 produced by Carbon Ukraine, Ltd, with particle size <40 µm.[75] $Ti_3C_2Cl_2$ was synthesized by molten salt etching of the same MAX phase precursor. HCl-washed dry Ti_3AlC_2 MAX phase (1 g) was immersed in etchant (20 mL) and stirred at 300 rpm at 35 °C for 24 h. The etching solution contains a mixture of HF (48-51 wt.%, Acros Organics), HCl (37 wt.%, Fisher Scientific), and DI water with a volumetric ratio of HF:HCl:H_2O equal to 1:6:3. Multilayered $Ti_3C_2T_x$ MXenes were intercalated with lithium chloride (LiCl, 99%, Alfa Aesar) using 1 g of LiCl per 1 g of Ti_3AlC_2 MAX, dissolved in DI water (50 mL), and stirred at 300 rpm at room temperature for 24 h. The resulting solution was washed with DI water and centrifuged at 3500 rpm for 5 min, followed by another DI water wash and centrifugation cycle. The supernatant was discarded, and the washed MXene was redispersed in propylene carbonate (99 wt.%, Sigma-Aldrich) by mechanical agitation in a paint shaker for 10 min. The dark supernatant was collected, and further cycles of redispersion in PC and mechanical agitation were repeated until a sufficient yield (30-50%) was reached.

Synthesis of $Ti_3C_2Cl_2$ MXene: For the synthesis of $Ti_3C_2Cl_2$ MXene, a molten salt etching process with anhydrous $ZnCl_2$ (Sigma Aldrich, >99%) as the etchant was used as previously reported.[15] $ZnCl_2$ and Ti_3AlC_2 MAX phase were mixed in a 1:8 mass ratio inside an Ar-filled glove box to prevent moisture contamination. The mixture was transferred to an alumina crucible and heated to 640 °C at a rate of 5 °C min^{-1} under constant Ar flow (5 SCCM) for 4 h. Following the reaction, the product was acid-washed in 12M HCl for 6 h to remove unreacted $ZnCl_2$ and Zn residues and then centrifuged at 1500 rcf for 5 min for several cycles with DI water to ensure thorough washing. The collected multilayer $Ti_3C_2Cl_2$ MXene was dried via vacuum filtration and transferred in a vacuum furnace for further drying at 45 °C for 48 h to remove surface adsorbed water. The completely dried MXene powders were transferred into the glovebox for future use. Delamination was achieved by intercalating Li^+ ions through the dissolution of anhydrous LiCl (1.2 g, Thermal Scientific Chemicals, 99.0%) in anhydrous dimethyl sulfoxide (DMSO, 10 mL, Sigma Aldrich, >99.9%) within a 20 mL glass vial inside an Ar-filled glove box.[15] Subsequently, multilayer $Ti_3C_2Cl_2$ (3 g) was added to the solution and stirred at 1000 rpm for 72 h to facilitate intercalation. The intercalated MXene was then washed twice with anhydrous tetrahydrofuran (THF, 10 mL, Sigma Aldrich, ≥99.9%), followed by additional washes with anhydrous N-methylformamide (NMF, Sigma Aldrich, >99.9%) at 1500 rcf for 5 min until swelling was observed. The swelled MXene was subsequently removed from the glovebox and dispersed into anhydrous propylene carbonate (45 mL). The dispersion was then subjected to bath sonication (Branson 2501 Ultrasonic Cleaner, 40 kHz) for 30 min, followed by centrifugation at 250 rcf for 5 min to obtain a stable colloidal suspension of delaminated MXene. To further concentrate the delaminated MXene, the suspension was centrifuged at 11200 rcf for 10 min.

Fabrication of PVDF-MXene Composite Films: Composites were fabricated by dissolving PVDF into solutions of MXene in PC. Dry PVDF powder (15 g, average M_W≈534000, Sigma-Aldrich) was weighed out in a glass jar, and a set mass of the PC-MXene solution was then added. The glass jar was placed in a bath of mineral oil at 110 °C to ensure the removal of any excess water and blended with an overhead stirrer at ≈200 rpm for 4–5 h to complete dissolution of the PVDF. The resultant polymer solution was kept heated until ready to be cast into films, as the PVDF will slowly phase out of the solution at lower temperatures. The solution was deposited onto a glass slide and blade coated at a thickness of 200 µm before submersion into a non-solvent bath of deionized water for at least 5 min to leach miscible PC out of the solution and create a free-standing film. This casting process is referred to as non-solvent induced phase separation (NIPS) and is commonly used to fabricate polymer membranes.[34,45] The free-standing films were removed from the water bath after 5–10 min to ensure solvent removal and left to dry at room temperature overnight. Dense, nonporous films were cast similarly, but doctor-bladed solutions were left in the air on a heated glass substrate at 150 °C for 2 h before non-solvent immersion. The resulting membranes were then studied for structure and material properties and fabricated into thin film capacitors.

Atomic Force Microscopy: AFM images were taken with a Bruker Dimension Icon microscope under ambient conditions, operating in Tapping Mode and using TESPA-V2 tips with a spring constant of k = 42 N m^{-1}. Images were captured at a scan rate of 1 Hz with 1024 lines per image. The statistical analysis was performed on 60 individual $Ti_3C_2T_x$ flakes, and the results were fitted using a lognormal distribution.

Scanning Electron Microscopy: SEM was performed using a Thermo Fisher Apreo 2S Lo Vac scanning electron microscope at an operating voltage of 10 kV and beam current of 0.20 nA. Images were captured using a secondary electron (SE) detector at magnifications from 120x to 50,000x. All samples were mounted on aluminum stubs with carbon tape. Nonconductive samples were sputter coated with a Pt/Pd layer using a Cressington Sputter Coater 208HR to deposit a 4–5 nm layer of conductive coating.

Focused ion beam-SEM was performed using a Tescan S8000X Xe plasma FIB-SEM at an operating voltage of 5 kV and beam current of 0.10 nA. FIB etching was done at a 55° angle using Xe plasma first at 10 nA and then at 1 nA for polishing. A combination of secondary electron (SE) and backscattered electron (BSE) detectors were used to capture images at magnifications from 120x to 100,000x.

X-Ray Computed Tomography: Micro-CT analysis was conducted using a Zeiss Versa 620 system at the Materials Characterization Core of Drexel University. The system operated at 50 kV and 4.5 W, utilizing a 20x objective to achieve a resolution of 0.6 µm. The sample was scanned at room temperature with 3000 projections without the use of any filters. Images were processed using Zeiss XRM Reconstructor software, including center shift adjustments and beam hardening, to ensure precise imaging. Further

image enhancement was carried out using Gaussian filtering to improve the quality. Segmentation and quantitative analysis were performed with ORS Dragonfly Pro software, employing a thresholding method refined by manual adjustments.

X-Ray Diffraction: Structural analysis was done using a Rigaku MiniFlex system at 40 kV and 15 mA with Cu Kα radiation. Samples were scanned from 3 to 65° with a step size of 0.02° and a scan speed of 4° min^{-1}. Both aqueous Ti_3AlC_2 MAX phase and $Ti_3C_2T_x$ MXene suspended in PC were dried into films or powder by vacuum-assisted filtration. PVDF and composite films were cut to size and secured with Kaptan tape.

Fourier Transform Infrared Spectroscopy: The FTIR was recorded using the KBr method. 0.001 g of each sample was mixed with 0.2 g of KBr powder (Sigma Aldrich, 99.99% anhydrous) followed by manual grinding in with agate mortar and pestle and pressed into pellets under 6 metric tons using hydraulic press (CarverTM) and dry pellet pressing die set (MSE Supplies). Plain KBr pellet is measured as background, and baseline correction is applied (concave rubberband correction, 6 iterations, 12 baseline points) with 25-point smoothing. The spectral resolution is 4 cm^{-1}, with 14 scans in total. All obtained data was normalized, so the sample's highest transmittance has the same value in each sample, resulting in arbitrary units (a. u.) of measurement.

Raman Spectroscopy: Inverted reflection mode Renishaw InVia spectrometer was used to collect Raman data using a 785 nm laser with a 1200 line per mm grating and 63× (NA = 0.7) objective. The acquisition time was 30 seconds, and the laser power was 3.59 mW to avoid sample degradation. The measurement was done using the free-standing films of PVDF-MXene and vacuum-filtered pristine MXene films. Spectra were normalized, and in some cases, background removal and smoothening were applied for peak clarity.

Dielectric Measurements: The free-standing films were cut into small pieces, and conductive silver paste was used to make electrodes on both sides. The average area of the electrodes of the capacitors varied between 300000 – 400000 mm^2. The dielectric properties of films were measured at room temperature by a HIOKI (3522) LCR tester with the sweeping frequency from 4 Hz to 7 MHz.

Capacitor Testing: Polarization (P-E loop) and breakdown voltage measurements were carried out under ambient conditions using a Radiant Technology Precession II Ferroelectric Tester with a High voltage (10kV) power source.

Supporting Information

Supporting Information is available from the Wiley Online Library or from the author.

Acknowledgements

This work was supported by the Air Force Research Laboratory (AFRL) and Balldyel Technologies Inc. SEM, XRD, and Micro-CT analyses were done with instruments in the Materials Characterization Core at Drexel University (RRID: SCR_022684 and MRI award number 2216175). FIB-SEM was carried out at the Singh Center for Nanotechnology, which was supported by the NSF National Nanotechnology Coordinated Infrastructure Program under grant NNCI-2025608. T.P. acknowledges support of U.S. National Science Foundation under grant CHE-2318105 (M-STAR CCI). S.B. and N.R.P. acknowledge support from Princeton Alliance for Collaborative Research and Innovation (PACRI) Grant #PACRI-JSU-02 and Army Research office under grant #W911NF-22-1-0281.

Conflict of Interest

The authors declare no conflict of interest.

Data Availability Statement

The data that support the findings of this study are available from the corresponding author upon reasonable request.

Keywords

dielectric capacitors, energy storage, MXenes, nanocomposites, polymer membranes, PVDF

Received: December 5, 2024
Revised: January 30, 2025
Published online: February 14, 2025

[1] S.-L. Zhong, Z.-M. Dang, W.-Y. Zhou, H.-W. Cai, *IET Nanodielectr.* **2018**, *1*, 41.
[2] P. Barber, S. Balasubramanian, Y. Anguchamy, S. Gong, A. Wibowo, H. Gao, H. J. Ploehn, H.-C. Zur Loye, *Materials* **2009**, *2*, 1697.
[3] Q. Li, F.-Z. Yao, Y. Liu, G. Zhang, H. Wang, Q. Wang, *Annu. Rev. Mater. Res.* **2018**, *48*, 219.
[4] W. Ji, G. Zhao, G. Hu, L. Fan, H. Deng, Q. Fu, *Compos. – A: Appl. Sci. Manuf.* **2021**, *149*, 106493.
[5] Z. Xie, D. Liu, X. Tang, Z. Fu, K. Wang, Q. Zhang, J. Wang, Q. Fu, *Compos. Sci. Technol.* **2023**, *232*, 109856.
[6] N. Meng, X. Ren, G. Santagiuliana, L. Ventura, H. Zhang, J. Wu, H. Yan, M. J. Reece, E. Bilotti, *Nat. Commun.* **2019**, *10*, 4535.
[7] N. Ismail, M. Essalhi, M. Rahmati, Z. Cui, M. Khayet, N. Tavajohi, *Green Chem.* **2021**, *23*, 2130.
[8] S. Biswas, S. Bhattacharya, *Thermochim. Acta* **2017**, *649*, 69.
[9] C. Kahrs, J. Schwellenbach, *Polymer* **2020**, *186*, 122071.
[10] L. Yang, J. Ho, E. Allahyarov, R. Mu, L. Zhu, *ACS Appl. Mater. Interfaces* **2015**, *7*, 19894.
[11] F. Guan, J. Pan, J. Wang, Q. Wang, L. Zhu, *Macromolecules* **2010**, *43*, 384.
[12] J. Jiang, Z. Shen, X. Cai, J. Qian, Z. Dan, Y. Lin, B. Liu, C.-W. Nan, L. Chen, Y. Shen, *Adv. Energy Mater.* **2019**, *9*, 1803411.
[13] Z. Bao, C. Hou, Z. Shen, H. Sun, G. Zhang, Z. Luo, Z. Dai, C. Wang, X. Chen, L. Li, Y. Yin, Y. Shen, X. Li, *Adv. Mater.* **2020**, *32*, 1907227.
[14] Y. Gogotsi, Q. Huang, *ACS Nano* **2021**, *15*, 5775.
[15] T. Zhang, K. Shevchuk, R. J. Wang, H. Kim, J. Hourani, Y. Gogotsi, *Chem. Mater.* **2024**, *36*, 1998.
[16] Y. Zhu, X. Zhao, Q. Peng, H. Zheng, F. Xue, P. Li, Z. Xu, X. He, *Nanoscale Adv.* **2021**, *3*, 5683.
[17] S. He, X. Sun, H. Zhang, C. Yuan, Y. Wei, J. Li, *Macromol. Rapid Commun.* **2021**, *42*, 2100324.
[18] W. Li, Z. Song, J. Zhong, J. Qian, Z. Tan, X. Wu, H. Chu, W. Nie, X. Ran, *J. Mater. Chem. C* **2019**, *7*, 10371.
[19] Y. Feng, Q. Deng, C. Peng, J. Hu, Y. Li, Q. Wu, Z. Xu, *J. Mater. Chem. C* **2018**, *6*, 13283.
[20] K. Maleski, V. N. Mochalin, Y. Gogotsi, *Chem. Mater.* **2017**, *29*, 1632.
[21] M. Malaki, A. Maleki, R. S. Varma, *J. Mater. Chem. A* **2019**, *7*, 10843.
[22] M. Carey, M. W. Barsoum, *Mater. Today Adv.* **2021**, *9*, 100120.
[23] M. Downes, C. E. Shuck, B. McBride, J. Busa, Y. Gogotsi, *Nat. Protoc.* **2024**, *19*, 1807.
[24] M. Alhabeb, K. Maleski, B. Anasori, P. Lelyukh, L. Clark, S. Sin, Y. Gogotsi, *Chem. Mater.* **2017**, *29*, 7633.
[25] A. Inman, K. Shevchuk, M. Anayee, W. Hammill, J. Lee, M. Saraf, C. E. Shuck, C. M. Armstrong, Y. He, T. Jin, M. Shekhirev, J. Capobianco, Y. Gogotsi, *J. Chem. Eng.* **2023**, *475*, 146089.
[26] A. Inman, V. Šedajová, K. Matthews, J. Gravlin, J. Busa, C. E. Shuck, A. VahidMohammadi, A. Bakandritsos, M. Shekhirev, M. Otyepka, Y. Gogotsi, *J. Mater. Res.* **2022**, *37*, 4006.

[27] M. Shekhirev, J. Busa, C. E. Shuck, A. Torres, S. Bagheri, A. Sinitskii, Y. Gogotsi, *ACS Nano* **2022**, *16*, 13695.
[28] S. Tu, Q. Jiang, J. Zhang, X. He, M. N. Hedhili, X. Zhang, H. N. Alshareef, *ACS Appl. Mater. Interfaces* **2019**, *11*, 27358.
[29] T. Habib, X. Zhao, S. A. Shah, Y. Chen, W. Sun, H. An, J. L. Lutkenhaus, M. Radovic, M. J. Green, *npj 2D Mater. Appl.* **2019**, *3*, 8.
[30] T. K. S. Fayaz, H. K. Chanduluru, R. H. Obaydo, P. Sanphui, *Sustain. Chem. Pharm.* **2024**, *37*, 101355.
[31] A. C. Y. Yuen, T. B. Y. Chen, B. Lin, W. Yang, I. I. Kabir, I. M. De Cachinho Cordeiro, A. E. Whitten, J. Mata, B. Yu, H.-D. Lu, G. H. Yeoh, *Compos. C: Open Access* **2021**, *5*, 100155.
[32] S. Tu, L. Qiu, C. Liu, F. Zeng, Y.-Y. Yuan, M. N. Hedhili, V. Musteata, Y. Ma, K. Liang, N. Jiang, H. N. Alshareef, X. Zhang, *ACS Nano* **2024**, *18*, 10196.
[33] L. Ruan, X. Yao, Y. Chang, L. Zhou, G. Qin, X. Zhang, *Polymers (Basel)* **2018**, *10*, 228.
[34] X. Tan, D. Rodrigue, *Polymers (Basel)* **2019**, *11*, 1160.
[35] J. Ji, F. Liu, N. A. Hashim, M. R. M. Abed, K. Li, *React. Funct. Polym.* **2015**, *86*, 134.
[36] J. Dong, Z. Li, C. Liu, B. Zhou, C. Liu, Y. Feng, *Nano Res.* **2024**, *17*, 5651.
[37] Y. Li, B. Zhou, Y. Shen, C. He, B. Wang, C. Liu, Y. Feng, C. Shen, *Compos. B: Eng.* **2021**, *217*, 108902.
[38] J. Zhang, N. Kong, S. Uzun, A. Levitt, S. Seyedin, P. A. Lynch, S. Qin, M. Han, W. Yang, J. Liu, X. Wang, Y. Gogotsi, J. M. Razal, *Adv. Mater.* **2020**, *32*, 2001093.
[39] X. Cai, T. Lei, D. Sun, L. Lin, *RSC Adv.* **2017**, *7*, 15382.
[40] Y. Barnakov, O. Paul, A. Joaquim, A. Falconer, R. Mu, V. Barnakov, D. Dikin, V. Petranovskii, A. Zavalin, A. Ueda, F. Williams, *Opt. Mater. Express* **2018**, *8*, 2579.
[41] K. Shevchuk, A. Sarycheva, C. E. Shuck, Y. Gogotsi, *Chem. Mater.* **2023**, *35*, 8239.
[42] E. Berger, Z.-P. Lv, H.-P. Komsa, *J. Mater. Chem. C* **2023**, *11*, 1311.
[43] X. Li, M. Li, X. Li, X. Fan, C. Zhi, *Research* **2022**, *2022*, 9892628.
[44] M. Krajewski, A. M. Witowski, S.-C. Liou, M. Maj, M. Tokarczyk, D. Wasik, *Macromol. Rapid Commun.* **2023**, *44*, 2300038.
[45] J. T. Jung, J. F. Kim, H. H. Wang, E. di Nicolo, E. Drioli, Y. M. Lee, *J. Membr. Sci.* **2016**, *514*, 250.
[46] H.-Q. Wang, J.-W. Wang, X.-Z. Wang, X.-H. Gao, G.-C. Zhuang, J.-B. Yang, H. Ren, *J. Chem. Eng.* **2022**, *437*, 135431.
[47] L. Padurariu, E. Brunengo, G. Canu, L. P. Curecheriu, L. Conzatti, M. T. Buscaglia, P. Stagnaro, L. Mitoseriu, V. Buscaglia, *ACS Appl. Mater. Interfaces* **2023**, *15*, 13535.
[48] X. Zhang, L. Zhang, M. Li, W. Chen, J. Chen, Y.-J. Liu, Y. Wang, *Membranes (Basel)* **2022**, *12*, 274.
[49] L. Wang, C. Liu, S. Shen, M. Xu, X. Liu, *Adv. Ind. Eng. Polym. Res.* **2020**, *3*, 138.
[50] M. Xie, M. Li, Q. Sun, W. Fan, S. Xia, W. Fu, *Mater. Sci. Semicond. Process.* **2022**, *139*, 106320.
[51] X. Liu, D. Lyu, C. Merlet, M. J. A. Leesmith, X. Hua, Z. Xu, C. P. Grey, A. C. Forse, *Science* **2024**, *384*, 321.
[52] Y. Li, Z.-Y. Fu, B.-L. Su, *Adv. Funct. Mater.* **2012**, *22*, 4634.
[53] Y. Li, J. Ho, J. Wang, Z.-M. Li, G.-J. Zhong, L. Zhu, *ACS Appl. Mater. Interfaces* **2016**, *8*, 455.
[54] Y. Fu, Y. Wang, S. Wang, Z. Gao, C. Xiong, *Polym. Compos.* **2019**, *40*, 2088.
[55] S. Bera, R. M. Thantirige, J. Wu, E. C. Davidson, S. A. Kadam, A. V. Sumant, B. T. Shook, R. Rao, R. Selhorst, M. Singh, A. Karim, D. Raghavan, N. R. Pradhan, *ACS Appl. Electron. Mater.* **2024**, *6*, 6582.
[56] J. Wang, Y. Xie, J. Liu, Z. Zhang, Y. Zhang, *Appl. Surf. Sci.* **2019**, *469*, 437.
[57] Z.-H. Shen, Z.-W. Bao, X.-X. Cheng, B.-W. Li, H.-X. Liu, Y. Shen, L.-Q. Chen, X.-G. Li, C.-W. Nan, *npj Comput. Mater.* **2021**, *7*, 110.
[58] H. Liu, J. Chen, J. Wang, Y. Sun, C. Wang, P. Zhang, Z. Shen, X. Zhang, B.-W. Li, C.-W. Nan, S. Zhang, *Mater. Today Energy* **2023**, *31*, 101213.
[59] J. Yang, H. Xie, H. Chen, Z. Shi, T. Wu, Q. Yang, C. Xiong, *J. Mater. Chem. A* **2018**, *6*, 1403.
[60] X. Peng, X. Liu, P. Qu, B. Yang, *J. Mater. Sci: Mater. Electron.* **2018**, *29*, 16799.
[61] X. Zhang, H. Chen, H. Ye, A. Liu, L. Xu, *Nanotechnology* **2020**, *31*, 165703.
[62] Y. Xie, J. Wang, Y. Yu, W. Jiang, Z. Zhang, *Appl. Surf. Sci.* **2018**, *440*, 1150.
[63] J. Wang, H. Chen, X. Li, C. Zhang, W. Yu, L. Zhou, Q. Yang, Z. Shi, C. Xiong, *J. Chem. Eng.* **2020**, *383*, 123147.
[64] J. Lao, H. Xie, Z. Shi, G. Li, B. Li, G.-H. Hu, Q. Yang, C. Xiong, *ACS Sustain. Chem. Eng.* **2018**, *6*, 7151.
[65] J. Chen, X. Zhang, Z. Wang, W. Chen, Q. Yuan, Y. Wang, *J. Mater. Chem. A* **2022**, *10*, 20402.
[66] L. Wu, K. Wu, D. Liu, R. Huang, J. Huo, F. Chen, Q. Fu, *J. Mater. Chem. A* **2018**, *6*, 7573.
[67] Q. Li, G. Zhang, F. Liu, K. Han, M. R. Gadinski, C. Xiong, Q. Wang, *Energy Environ. Sci.* **2015**, *8*, 922.
[68] H. Li, L. Ren, D. Ai, Z. Han, Y. Liu, B. Yao, Q. Wang, *InfoMat* **2020**, *2*, 389.
[69] F. Liu, Q. Li, Z. Li, L. Dong, C. Xiong, Q. Wang, *Compos. A: Appl. Sci. and Manuf.* **2018**, *109*, 597.
[70] M. Singh, P. Das, P. N. Samanta, S. Bera, R. Thantirige, B. Shook, R. Nejat, B. Behera, Q. Zhang, Q. Dai, A. Pramanik, P. Ray, D. Raghavan, J. Leszczynski, A. Karim, N. R. Pradhan, *ACS Nano* **2023**, *17*, 20262.
[71] J. Li, J. Zhang, S. Zhang, K. Ren, *Macromol. Mater. Eng.* **2021**, *306*, 2100079.
[72] D. Cheng, H. Wang, B. Liu, S. Wang, Y. Li, Y. Xia, C. Xiong, *J. Appl. Polym. Sci.* **2019**, *136*, 47991.
[73] Q. Jia, X. Huang, G. Wang, J. Diao, P. Jiang, *J. Phys. Chem. C* **2016**, *120*, 10206.
[74] S. Yu, C. Ding, Y. Liu, Y. Liu, Y. Zhang, H. Luo, D. Zhang, S. Chen, *J. Power Sources* **2022**, *535*, 231415.
[75] T. S. Mathis, K. Maleski, A. Goad, A. Sarycheva, M. Anayee, A. C. Foucher, K. Hantanasirisakul, C. E. Shuck, E. A. Stach, Y. Gogotsi, *ACS Nano* **2021**, *15*, 6420.

